Hybrid Thermal-Nonthermal Synchrotron Emission from Hot Accretion Flows

Feryal Özel[1], Dimitrios Psaltis, and Ramesh Narayan
Harvard-Smithsonian Center for Astrophysics, 60 Garden Street, Cambridge, MA 02138;
fozel,dpsaltis,rnarayan@cfa.harvard.edu

ABSTRACT

We investigate the effect of a hybrid electron population, consisting of both thermal and non-thermal particles, on the synchrotron spectrum, image size, and image shape of a hot accretion flow onto a supermassive black hole. We find two universal features in the emitted synchrotron spectrum: (i) a prominent shoulder at low ($\lesssim 10^{11}$ Hz) frequencies that is weakly dependent on the shape of the electron energy distribution, and (ii) an extended tail of emission at high ($\gtrsim 10^{13}$ Hz) frequencies whose spectral slope depends on the slope of the power-law energy distribution of the electrons. In the low-frequency shoulder, the luminosity can be up to two orders of magnitude greater than with a purely thermal plasma even if only a small fraction ($< 1\%$) of the steady-state electron energy is in the non-thermal electrons. We apply the hybrid model to the Galactic center source, Sgr A*. The observed radio and IR spectra imply that at most 1% of the steady-state electron energy is present in a power-law tail in this source. This corresponds to no more than 10% of the electron energy injected into the non-thermal electrons and hence 90% into the thermal electrons. We show that such a hybrid distribution can be sustained in the flow because thermalization via Coulomb collisions and synchrotron self-absorption are both inefficient.

The presence of non-thermal electrons enlarges the size of the radio image at low frequencies and alters the frequency dependence of the brightness temperature. A purely thermal electron distributions produces a sharp-edged image while a hybrid distribution causes strong limb brightening. These effects can be seen up to frequencies $\sim 10^{11}$ Hz and are accessible to radio interferometers.

Subject headings: accretion, accretion flows – black hole physics – radiation mechanisms: thermal and non-thermal synchrotron – Galaxy: center

To appear in *The Astrophysical Journal*

[1]Physics Department, Harvard University

1. Introduction

The mechanisms of particle heating and acceleration, and the emission spectra from the resulting particle energy distributions, are of great importance in the theory of collisionless hot accretion flows onto compact objects. Discussions in the literature have focused on the physics of electron heating and acceleration (Begelman & Chiueh 1988; Bisnovatyi-Kogan & Lovelace 1997; Quataert & Gruzinov 1999; Gruzinov & Quataert 1999, Medvedev 2000), the efficiency of particle thermalization (Ghisellini, Guilbert, & Svensson 1988; Ghisellini, Haardt, & Fabian 1993; Mahadevan & Quataert 1997; Ghisellini, Haardt, & Svensson 1998; Nayakshin & Melia 1998), and the generation of hybrid thermal-nonthermal electron energy distributions in these plasmas (see, e.g., Coppi 1999 and references therein). Despite a substantial amount of work, many issues remain unresolved, primarily because of our incomplete understanding of physical processes such as magnetic reconnection, MHD turbulence, and collective plasma modes.

These questions are especially relevant for an optically-thin advection-dominated accretion flow (ADAF). An ADAF is an example of a hot, rarefied, magnetic plasmas with low radiative efficiency (Ichimaru 1977; Narayan & Yi 1994, 1995b; Abramowicz et al. 1995; see Narayan, Mahadevan, & Quataert 1998b and Kato, Fukue, & Mineshige 1998 for reviews). A basic property of the nearly collisionless plasma in an ADAF is that the Coulomb coupling between the electrons and ions is weak so that energy transfer from the ions to the electrons is inefficient. In addition, it is commonly assumed that the viscously generated energy primarily heats the heavier species, the ions, and that the electrons retain a thermal distribution throughout the flow (e.g., Narayan & Yi 1995b; Mahadevan 1997).

There are, however, processes such as MHD turbulence, pair production (e.g., through pion decay), and electron-proton coupling which can both heat the electrons and generate non-thermal distributions. Quataert and Gruzinov (1999; see also Gruzinov & Quataert 1999) considered two processes specific to MHD turbulence that accelerate particles in magnetic collisionless plasmas: Landau damping by electric fields parallel to the local magnetic field and transit-time damping by time-varying magnetic fields. They found that the assumption of negligible electron heating/acceleration is valid only for weak magnetic fields, i.e., when the ratio of the gas pressure to total pressure $\beta_{\rm ADAF}$ is larger than a critical value $\beta_{\rm crit}$. The value of $\beta_{\rm crit}$ is very uncertain and is around 0.9. For $\beta_{\rm ADAF} \gtrsim 0.9$, turbulence primarily accelerates the protons, while for stronger magnetic fields, the results are inconclusive. Shocks and pion decay can also lead to non-thermal electrons in the accretion flow.

Several processes, such as Coulomb collisions and synchrotron self-absorption, can potentially lead to thermalization of particles in accretion flows (Mahadevan & Quataert 1997; Ghisellini et al. 1998). Mahadevan & Quataert (1997) showed that Coulomb collisions are ineffective in thermalizing the electrons in an ADAF. However, they argued that, for sufficiently high mass-accretion rates, the electrons in the plasma can be thermalized by synchrotron self-absorption. Nayakshin and Melia (1998) showed that considerable deviations from a Maxwell-Boltzmann

distribution can be sustained in a plasma with low source compactness when Coulomb collisions, Comptonization, and pair processes are taken into account.

In view of the difficulty of calculating the heating, cooling and thermalization of particles from first principles, many authors have restricted their models to either purely Maxwellian or purely non-thermal (extended power laws or monoenergetic) electron distributions. Only recently have there been attempts towards explaining spectra of accreting black holes with models including hybrid thermal/non-thermal distributions of electrons. Some models have physically motivated distributions, such as non-thermal electrons produced by decaying pions (Mahadevan 1998), whereas others invoke more *ad hoc* distributions to fit the data (e.g., Beckert & Duschl 1997; Falcke & Biermann 1999). The reverse process of trying to constrain the energy distributions of particles in accreting plasmas by comparing models to data, however, faces issues of uniqueness which can be addressed only by a more comprehensive study of hybrid models.

In this paper, we consider generalized electron distributions consisting of a dominant Maxwellian plus a small non-thermal power-law component of varying slope and energy content, and study the synchrotron emission from the resulting hybrid plasmas. We identify the characteristic signatures of the non-thermal electrons on the emitted radio synchrotron spectrum of an accretion flow and on its image as observed with a radio telescope. We also discuss to what extent the observed effects could be used to determine the details of the underlying non-thermal electron distribution. This work is relevant for interpreting observations of low luminosity AGNs such as the Galactic Center source, Sagittarius A* (Sgr A*).

In §2 we review the basic properties of ADAFs, hybrid plasmas, synchrotron radiation, and radiative transfer. In §3 we present a series of models of supermassive black holes with low accretion rates. We apply these models to Sgr A* and derive constraints on the fraction of the electron energy that can be present in a non-thermal form. In §4, we study the correspondence between the energy distribution of the electrons and the resulting spectrum. In §5 we study the energetics of a hybrid flow and calculate the heating, cooling and thermalization rates of the non-thermal electrons. We summarize our conclusions in §6. We present in an Appendix approximate analytic expressions for the contribution of a non-thermal particle population to the synchrotron spectrum of an accretion flow.

2. Formalism

2.1. Advection-Dominated Flows

We begin by reviewing some of the basic properties of the optically-thin branch of ADAFs. ADAFs are quasi-spherical, hot, magnetic accretion flows in which the accreting plasma is too rarefied to cool efficiently by radiative processes. The viscously dissipated energy is therefore advected into the black hole or other compact object at the center (see Narayan et al. 1998b

and Kato et al. 1998 for reviews). In the limit where the fraction of the viscous energy advected inward is independent of radius, a self-similar analytic solution for the thermodynamic quantities of the accreting gas can be obtained (Narayan & Yi 1994, 1995b). We make use of this solution in Appendix A. For the numerical calculations presented in the rest of the paper, we use more accurate global solutions to obtain the run of electron temperature and density with radius. These solutions are calculated by the methods described in Narayan, Kato, & Honma (1997b), Chen, Abramowicz, & Lasota (1997), and Popham & Gammie (1998). The magnetic field strengths are obtained by assuming that the ratio of gas pressure to total pressure (sum of gas and magnetic pressure) is equal to a specified value $\beta_{\rm ADAF}$.

Since the focus of this paper is on massive black holes in galactic nuclei with low mass-accretion rates, with specific applications to the black hole in our own Galactic nucleus, Sgr A*, we scale masses in units of 10^6 solar mass, i.e., $M \equiv m_6 10^6 M_\odot$, and radii in units of the Schwarzschild radius, i.e., $R \equiv r R_{Sch}$, where

$$R_{Sch} = \frac{2GM}{c^2} = 2.95 \times 10^{11} m_6 \text{ cm}. \tag{1}$$

We scale the mass accretion rate in units of $10^{-3}\dot{M}_{\rm Edd}$, i.e., $\dot{M} \equiv \dot{m}_{-3} 10^{-3} \dot{M}_{\rm Edd}$, where the Eddington mass accretion rate is

$$\dot{M}_{\rm Edd} = \frac{L_{\rm Edd}}{\eta_{\rm eff} c^2} = 1.39 \times 10^{24} \left(\frac{\eta_{\rm eff}}{0.1}\right)^{-1} m_6 \text{ g s}^{-1}. \tag{2}$$

In defining the Eddington rate, we assume a standard radiative efficiency of $\eta_{\rm eff} = 0.1$. (This is purely for the purposes of the definition; the actual radiative efficiency can be very different from 0.1).

For the calculations presented here we use ADAF models in which the viscosity parameter is set to $\alpha = 0.1$, the equipartition parameter to $\beta_{\rm ADAF} = 0.968$, and the ratio of viscous electron heating to proton heating to $\delta = 10^{-3}$. Note that $\beta_{\rm ADAF}$ differs from the usual plasma parameter β, which is the ratio of the gas pressure to the magnetic pressure; the value of $\beta_{\rm ADAF} = 0.968$ assumed in our ADAF models corresponds to a plasma $\beta = 10$ (Quataert & Narayan 1999).

2.2. Hybrid Populations

We assume that a large fraction of the electrons in the plasma are in a thermal distribution with temperature T and that the rest of the electrons are in a non-thermal distribution, usually with a power-law form. We denote the number density of electrons in the thermal population by $N_{\rm th}$ and in the non-thermal population by $N_{\rm pl}$. We denote the emissivities of the thermal and power-law electron populations by $j_{\rm th}$ and $j_{\rm pl}$ respectively, and the corresponding absorption coefficients by $\alpha_{\rm th}$ and $\alpha_{\rm pl}$.

For the thermal electron population, we use the relativistic Maxwell-Boltzmann distribution given by

$$n_{\rm th}(\gamma) = N_{\rm th}\gamma^2\beta{\rm exp}(-\gamma/\theta_{\rm e})/[\theta_{\rm e}{\rm K}_2(1/\theta_{\rm e})], \tag{3}$$

where γ is the electron Lorentz factor, β is the relativistic electron velocity, and $\theta_e \equiv kT/m_ec^2$ is the dimensionless electron temperature. The modified Bessel function of second order $K_2(1/\theta_e)$ arises from the normalization of the Maxwellian. Similarly, for the non-thermal electron population we use a power-law distribution extending from $\gamma = 1$ to infinity,

$$n_{\rm pl}(\gamma) = N_{\rm pl}(p-1)\gamma^{-p}. \tag{4}$$

The number density of thermal electrons $N_{\rm th}$ is a function of the flow radius and is determined by the global ADAF solutions. We determine $N_{\rm pl}$ at each radius by assuming that the steady-state energy in the non-thermal distribution is equal to a fraction η of the energy in the thermal distribution, with η constant in radius. Although the calculations presented in §3 are all carried out with this assumption, generalizations to radially-dependent $\eta(r)$ as well as a discussion of the energetics of such a flow will be presented in §5. Note that we implicitly assume that the non-thermal electron population does not affect the dynamics or the thermal properties of the flow; this will be justified in §5.

The energy density of a Maxwell-Boltzmann distribution of electrons at temperature θ_e was derived by Chandrasekhar (1939, eq. [236]) to be

$$u = a\left(\theta_e\right) N_{\rm th} m_e c^2 \theta_e, \tag{5}$$

where

$$a\left(\theta_e\right) \equiv \frac{1}{\theta_e}\left[\frac{3K_3(1/\theta_e) + K_1(1/\theta_e)}{4K_2(1/\theta_e)} - 1\right] \tag{6}$$

is a coefficient that varies from 3/2 for a non-relativistic electron gas to 3 for fully relativistic electrons, and K_n are the modified Bessel functions of the nth order. For the present purposes, we use a simplified expression for $a(\theta_e)$ which has an error of less than 2% at all temperatures (Gammie & Popham 1998):

$$a(\theta_e) = \frac{6 + 15\theta_e}{4 + 5\theta_e}. \tag{7}$$

The number density of the non-thermal distribution is then

$$N_{\rm pl} = \eta a(\theta_e)\theta_e(p-2)N_{\rm th}. \tag{8}$$

This normalization of the power law population typically corresponds to

$$\frac{N_{\rm pl}}{N_{\rm th}} \sim (0.1 - 10)\eta, \tag{9}$$

depending on the electron temperature and the power law index.

The distributions considered above correspond to the steady state that results from the competition between heating/acceleration and cooling by radiation. We discuss in some detail in §5 the energy equations for the thermal and non-thermal electron populations. Here we simply note that the synchrotron cooling timescale of electrons moving with a Lorentz factor γ scales as γ^{-2}, and hence electrons in the high energy tail of a power law distribution cool most rapidly. As a result, if electrons are injected with a power-law distribution with index s [$n(\gamma) \propto \gamma^{-s}$] and cool only by synchrotron emission, the synchrotron cooling causes the power law index of the steady state distribution to be $p = s + 1$ above a certain γ_b, called the cooling break, thus causing the steady state distribution to fall off more steeply at higher electron energies. Mahadevan & Quataert (1997) calculated γ_b in an ADAF by comparing the cooling timescale to the inflow timescale and found that at sufficiently high accretion rates, the break occurs at a very low Lorentz factor, $\gamma_b \sim 1.5$. The Lorentz factors of interest to us are invariably larger than γ_b. Therefore, the values of p we consider below in §3 and §4 are always equal to $s + 1$, so that the injected energy distribution γ^{-s} is harder by one power of γ than the steady state energy distribution, γ^{-p}.

Corresponding to η, we can define another quantity $\eta_{\rm inj}$ that measures the fraction of electron energy *injected* into a power law distribution. If $s < 2$, then $\eta_{\rm inj}$ can be significantly greater than η. If we assume a distribution from $\gamma_{\rm min} = 1$ to some $\gamma_{\rm max}$, $\eta_{\rm inj}$ is greater than η by a factor $\sim \gamma_{\rm max}^{3-p}$. However, it is thought that the acceleration mechanisms typically encountered in astrophysics, such as shock acceleration or acceleration via MHD turbulence, inject energy into particles with $s > 2$ such that the steady state distribution has $p > 3$. In this case there is little dependence on $\gamma_{\rm max}$, and

$$\frac{\eta_{\rm inj}}{\eta} \simeq \frac{p-2}{p-3}, \tag{10}$$

which is not very different from unity. Although we expect $s > 2$ and $p > 3$ for most systems, for completeness we consider models in the range $2 < p < 4$.

2.3. Synchrotron Emissivity

The synchrotron emissivity of a relativistic electron moving with a Lorentz factor γ in a magnetic field of strength B is given by (Rybicki & Lightman 1979)

$$j_\nu(\gamma, \theta) = \frac{\sqrt{3}e^2}{2c}\nu_b \sin\theta F(x). \tag{11}$$

Here, $\nu_b \equiv eB/2\pi m_e c$ is the non-relativistic cyclotron frequency, θ is the angle between the direction of the magnetic field and the velocity of the electron, and

$$F(x) \equiv x \int_x^\infty K_{5/3}(t)dt, \tag{12}$$

with $K_{5/3}$ the modified Bessel function of order 5/3, $x \equiv \nu/\nu_c$, and $\nu_c \equiv \frac{3}{2}\gamma^2\nu_b \sin\theta$. For a thermal distribution of electrons, the total emissivity for a given angle θ is obtained by integrating equation

(11) over the Maxwellian distribution (Pacholczyk 1970),

$$j_{\nu,\rm th}(\theta) = \frac{N_{\rm th}e^2}{\sqrt{3}cK_2(1/\theta_e)}\nu I\left(\frac{x_M}{\sin\theta}\right), \tag{13}$$

where

$$x_M \equiv \frac{2\nu}{3\nu_b\theta_e^2} \tag{14}$$

and

$$I(x_M) \equiv \frac{1}{x_M}\int_0^\infty z^2\exp(-z)F(x_M/z^2)dz. \tag{15}$$

The limiting behaviour of $I(x_M)$ for small and large x_M was derived by Pacholczyk (1970) and Petrosian (1981), respectively. Mahadevan, Narayan, & Yi (1996, hereafter MNY96) integrated equation (13) over the angle θ for an isotropic distribution of electron velocities and provided a fitting function for the emissivity in the ultrarelativistic to mildly relativistic regimes:

$$j_{\nu,\rm th} = \frac{N_{\rm th}e^2}{\sqrt{3}cK_2(1/\theta_e)}\nu M(x_M), \tag{16}$$

with $M(x_M)$ given by

$$M(x_M) = \frac{4.0505\ a}{x_M^{1/6}}\left(1+\frac{0.40\ b}{x_M^{1/4}}+\frac{0.5316\ c}{x_M^{1/2}}\right)\exp(-1.8896x_M^{1/3}). \tag{17}$$

The best fit values of the coefficients a, b, and c for different temperatures are given in MNY96. The coefficients tend to unity in the ultrarelativistic limit. Finally, the synchrotron absorption coefficient $\alpha_{\rm th}$ is related to the emissivity via Kirchoff's law,

$$\alpha_{\nu,\rm th} = j_{\nu,\rm th}/B_\nu(T), \tag{18}$$

where $B_\nu(T)$ is the black body source function.

For the total emissivity of electrons in a power law distribution, we use the expression given in Rybicki & Lightman (1979) and average over angles,

$$j_{\nu,\rm pl} = C_{\rm pl}^j\eta\frac{e^2N_{\rm th}}{c}a(\theta_e)\theta_e\nu_b\left(\frac{\nu}{\nu_b}\right)^{(1-p)/2}, \tag{19}$$

where $N_{\rm pl}$ is defined in terms of $N_{\rm th}$ as above and

$$C_{\rm pl}^j = \frac{\sqrt{\pi}3^{p/2}}{4}\frac{(p-1)(p-2)}{(p+1)}\frac{\Gamma(\frac{p}{4}+\frac{19}{12})\Gamma(\frac{p}{4}-\frac{1}{12})\Gamma(\frac{p}{4}+\frac{5}{4})}{\Gamma(\frac{p}{4}+\frac{7}{4})}. \tag{20}$$

The corresponding absorption coefficient is

$$\alpha_{\nu,\rm pl} = C_{\rm pl}^\alpha\eta\frac{e^2N_{\rm th}}{c}a(\theta_e)\theta_e\left(\frac{\nu_b}{\nu}\right)^{(p+3)/2}\nu^{-1}, \tag{21}$$

with

$$C_{\rm pl}^\alpha = \frac{\sqrt{3\pi}3^{p/2}}{8}\frac{(p-1)(p-2)}{m_e}\frac{\Gamma(\frac{3p+2}{12})\Gamma(\frac{3p+22}{12})\Gamma(\frac{6+p}{4})}{\Gamma(\frac{8+p}{4})}. \tag{22}$$

2.4. Radiative Transfer and Numerical Methods

The equation of radiative transfer for a time-independent, spherically symmetric flow is (e.g., Mihalas 1978)

$$\mu(\partial/\partial r) + r^{-1}(1-\mu^2)(\partial/\partial\mu)]I(r,\mu,\nu) = j(r,\nu) - \alpha(r,\nu)I(r,\mu,\nu), \tag{23}$$

where $\mu \equiv \cos\theta = (dz/ds)$ is the cosine of the angle between the ray and the radial direction, r is the radial coordinate, ν is the frequency, and j and α are the emission and absorption coefficients defined above. One can simplify this equation by taking plane parallel rays of varying impact parameters (perpendicular distances of rays to the central line of sight) through the flow and solving the equation along these rays (Mihalas 1978). The equation then becomes

$$\pm \frac{\partial I_\nu^\pm}{\partial s} = j_\nu - \alpha_\nu I_\nu^\pm, \tag{24}$$

where now s is the line element along the ray and the coefficients $+1$ and -1 correspond to radiation coming towards and going away from an external observer, respectively. In our problem, $j_\nu = j_{\rm th} + j_{\rm pl}$ and $\alpha_\nu = \alpha_{\rm th} + \alpha_{\rm pl}$. Rewriting the equation in terms of the source function $S_\nu = j_\nu/\alpha_\nu$ and optical depth $\tau(s) = -\int_s^{s_{out}} \alpha ds'$, where s_{out} is the point of intersection of the ray with the outer boundary of the flow, equation (24) becomes

$$\pm \frac{\partial I_\nu}{\partial \tau} = I_\nu - S_\nu, \tag{25}$$

where the combined source function is

$$S_\nu = \frac{j_\nu}{\alpha_\nu} = \frac{j_{\rm th} + j_{\rm pl}}{\alpha_{\rm th} + \alpha_{\rm pl}} = \frac{S_{\rm th}}{1 + \alpha_{\rm pl}/\alpha_{\rm th}} + \frac{S_{\rm pl}}{1 + \alpha_{\rm th}/\alpha_{\rm pl}}. \tag{26}$$

In the numerical calculations reported below, we integrate equation (25) using the formal solution and the appropriate boundary conditions for a non-illuminated atmosphere (see Mihalas 1978). We carry out the integral along rays with impact parameters up to ~ 2000 Schwarzschild radii, beyond which the temperature of the electrons becomes too low for significant synchrotron emission. Because of the very steep dependence of the synchrotron emissivity on photon frequency, magnetic field strength, and electron temperature and density, we use an adaptive step size for the radiative transfer integral. The total flux is obtained by integrating over all impact parameters. We validated the implementation of our numerical algorithm by comparing its output to analytic solutions of the radiative transfer equation in uniform media. The discrepancy between the numerical and analytic solutions was $\lesssim 0.5\%$ for the cases considered.

In all model ADAF spectra published so far, the transport of radiation has been calculated using an approximate method based on concentric shells (Narayan, Barret, & McClintock 1997a). In Figure 1, we compare, for a typical flow, the exact spectrum obtained by formally solving the above transfer equation to that obtained with the previous approximate method. We see that

there is a fairly good agreement between the two methods, but with some differences. The most prominent difference is a shifting of the peak toward higher frequencies in the exact calculation, as well as some broadening. This is probably due to the poorer resolution of the concentric shell method which becomes a limiting factor close to the black hole. There is also a slight offset at lower frequencies, probably again due to poor resolution. Note that there is a second peak at high frequencies ($\gtrsim 10^{14}$ Hz) in the spectrum calculated with the approximate method. This is caused by the inverse Compton scattering of soft photons, a process which is not included in the radiative transfer code described here. The remaining features of the two spectra are quantitatively consistent.

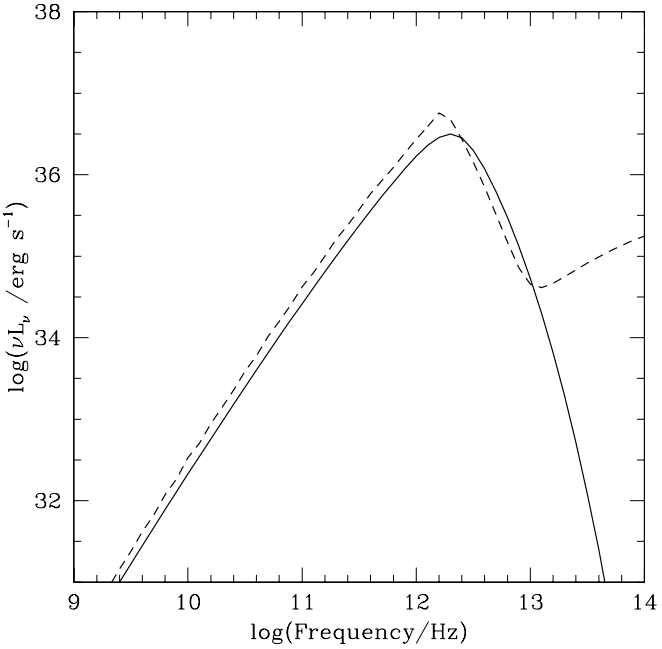

Fig. 1.— The solid line shows a typical spectrum calculated with the radiative transfer method employed in this paper. The model parameters are those used for Sgr A*: $m_6 = 2.5$, $\dot{m}_{-3} = 0.1$, and other ADAF parameters as specified in the text. The dashed line is an approximate spectrum of the same model, calculated by a simplified method described in Narayan et al. (1997a). The secondary rise at $\nu \gtrsim 10^{13}$ Hz is due to Compton scattering, which is not included in the exact calculation.

3. Numerical Results

3.1. Parameter Study

In this section, we study the effects of an extended power-law electron distribution on the synchrotron emission spectra of ADAFs. Figure 2 shows the various components of the spectrum of a typical hybrid model, with $p = 3.5$, $\eta = 1\%$, $m_6 = 2.5$, and $\dot{m}_{-3} = 1$. Compared to the

spectrum of a pure thermal model (dashed line), we see two primary effects due to the power-law electrons: (i) there is a prominent shoulder of optically thick emission at low frequencies and (ii) there is an extended power-law tail of optically thin emission at high frequencies. In between these two features there is a region of the spectrum where the thermal peak dominates. These features were first identified by Mahadevan (1998) for a specific model. We find that they are universal for hybrid models.

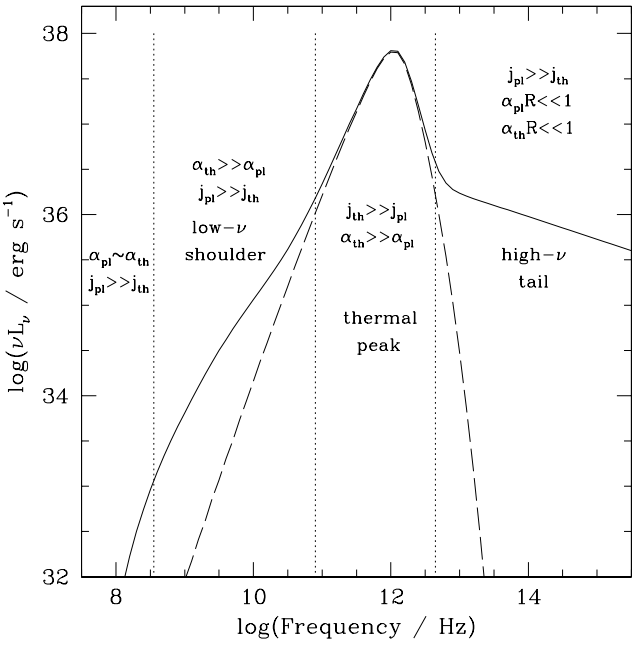

Fig. 2.— Regions of a hybrid synchrotron spectrum labeled according to the dominant emitting and absorbing electron population and the resulting spectral shape. The different segments and the transitions are present in all hybrid synchrotron spectra.

To understand the results, we note that the spectra of hybrid populations are determined by a competition between $j_{\rm pl}$ and $j_{\rm th}$ and between $\alpha_{\rm pl}$ and $\alpha_{\rm th}$, each having different radial and frequency dependences. Since the emission at different frequencies arises from different radii in the flow, the relative importance of $\alpha_{\rm pl}$ to $\alpha_{\rm th}$ and $j_{\rm pl}$ to $j_{\rm th}$ at that particular frequency and radius determines the local behaviour of the spectrum. In the less steep segment of the low-frequency shoulder, the emission from the power-law population (which is more efficient at low frequencies) exceeds that of the thermal electrons, while absorption is still mostly dominated by the more numerous thermal electrons. As a result, this segment of the spectrum assumes a shape roughly described by the rather unusual source function $S = j_{\rm pl}/\alpha_{\rm th}$. At still lower frequencies, where the emission comes from larger radii in the flow, the contribution of the non-thermal electrons to the absorption becomes non-negligible and the spectrum falls more steeply with decreasing ν.

In the region of the thermal peak, we have both $j_{\rm th} \gg j_{\rm pl}$ and $\alpha_{\rm th} \gg \alpha_{\rm pl}$, with $\alpha_{\rm th} R \gg 1$

for frequencies smaller than the peak frequency and $\alpha_{\rm th}R \ll 1$ for frequencies higher than the peak frequency. The spectrum is essentially the same as for a purely thermal model (dashed line). (But, note that for sufficiently high η, the synchrotron spectrum assumes an entirely non-thermal character and this region too can be dominated by the power-law electrons, with the peak luminosity becoming higher and the peak flattened). Beyond the thermal peak, there is no self-absorption either by thermal or power-law electrons ($\alpha_{\rm th}R, \alpha_{\rm pl}R \ll 1$) and the emission is optically thin. Here we find an extended power-law tail dominated entirely by the non-thermal population. This segment of the spectrum has the familiar form $\nu L_\nu \sim \nu^{-(p-3)/2}$ which gives a rising spectrum with increasing frequency for $p < 3$ and a falling spectrum for $p > 3$.

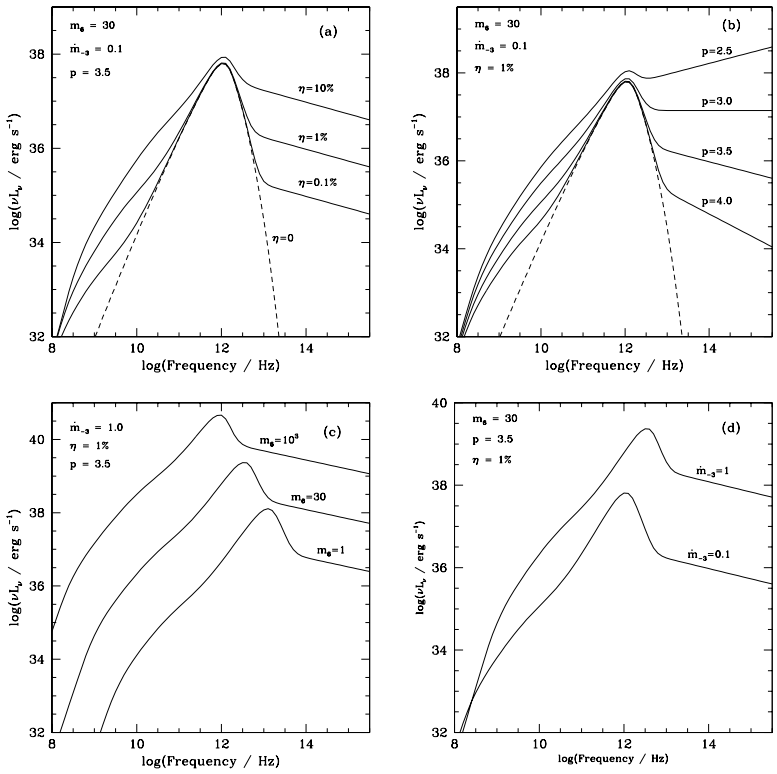

Fig. 3.— Variations in the synchrotron spectrum as a function of (a) the fraction of non-thermal energy content η, (b) the power-law index p, (c) the black hole mass in units of $10^6 M_\odot$, and (d) the mass-accretion rate in units of $10^{-3}\dot{M}_{\rm Edd}$.

Figures 3a-d show how the spectrum of a hybrid model depends on the various parameters. In Figure 3a, the energy content of the power-law population η is varied from 0% (purely thermal) to 10%; we see that the range and normalization of the low-frequency shoulder increase linearly with increasing η. The normalization of the high-frequency tail also depends linearly on the number of electrons in the power-law distribution and thus varies in an obvious way with η.

In Figure 3b, we fix η at 1% and vary the power-law index p. Note that the overall luminosity

of both the low-frequency shoulder and the high-frequency tail show considerable dependence on p. This is not unexpected. When p is small, there are more particles both at intermediate Lorentz factors ($\log\gamma = 1-2$), which give rise to the low-frequency shoulder, as well as at large γ, which emit the high-frequency tail (see §4). Therefore, small values of p give more emission in both these segments of the spectrum. The high-frequency tail has a spectral slope equal to $-(p-3)/2$ and therefore has a strong dependence on p.

Two striking qualitative results in Figures 3a and 3b need to be highlighted. First, even very small values of the non-thermal energy content η give rise to significant excess super-thermal emission at low frequencies. For instance, even if only 1% of the total electron energy is in non-thermal electrons, there can be several orders of magnitude higher luminosity at frequencies below the thermal peak. Even more striking is the fact that the spectral shape of the low frequency shoulder is nearly independent of η and p, when both these parameters are independent of radius, while the normalization depends on both (see Appendix A for an analytic expression for the spectral slope of this segment). This leads to a degeneracy between η and p in models of the low-frequency emission, so that it is not possible to distinguish between different combinations of η and p, by studying spectral data below the thermal peak only. The degeneracy can be lifted with data on the high-frequency tail whose slope has a strong dependence on p.

We finally consider the effect of changing the black hole mass and the mass-accretion rate. We find that the relative excess emission due to non-thermal electrons increases rather weakly with increasing black hole mass (Figure 3c). This is because the thermal peak moves to lower frequencies for higher m_6 (Mahadevan 1997) and at these frequencies the effect of non-thermal electrons is more prominent. The non-thermal contribution to both the low and high frequency emission increases only weakly with increasing $\dot{m}_{-3}$ (Figure 3d).

3.2. Application to Sgr A*

Over the last decade, many models have been developed to explain the radio spectrum of Sgr A*. This source is believed to be an accreting supermassive black hole at the center of our Galaxy. Nearly all the published models invoke synchrotron radiation from relativistic or quasi-relativistic electrons. Melia (1992) considered emission by thermal electrons in a spherical accretion flow and showed that the resulting cyclo-synchrotron emission is consistent with the broad features of the observed spectrum. Narayan, Yi, & Mahadevan (1995) and Narayan et al. (1998a) developed ADAF models of Sgr A* which included rotation, viscosity and a two-temperature plasma, and obtained similar results, again with a purely thermal distribution of electrons. Beckert & Duschl (1997) and Falcke & Biermann (1999) considered non-thermal models, while Mahadevan (1998) analyzed a specific hybrid model in which the non-thermal electrons are produced by pion decay. This section is a generalization of Mahadevan's work.

In Figure 4 we apply our hybrid emission model to Sgr A*. We take $m_6 = 2.5$ (Eckart &

Genzel 1997; Ghez et al. 1998) and adjust $\dot{m}_{-3}$ in order to fit approximately the thermal peak. The data shown are the same as in Narayan et al. (1998a). Figure 4 shows four models with $p = 2.5$, $\eta = 0.05\%$; $p = 3.0$, $\eta = 0.2\%$; $p = 3.5$, $\eta = 0.5\%$; and $p = 4.0$, $\eta = 1\%$. We first note that the agreement with data at low frequencies is significantly better with these hybrid models (dashed lines) than with a purely thermal model (solid line), as was first shown by Mahadevan (1998).

The two major results pointed out in §3.1 are evident in this figure. First, there is no unique solution for the parameters p and η. The four hybrid models shown in Figure 4 give indistinguishable spectra below the thermal peak, rendering it impossible to determine p and η from low-frequency spectral data alone. Second, η is extremely small in all models. A very small fraction of the energy in non-thermal electrons, with η at most 1%, is sufficient to produce all the observed emission at low frequencies. This means that the non-thermal electrons are a minor perturbation on the electron population, which is itself a minor perturbation on the more dominant ion population. We are therefore consistent when we compute the gas dynamics with a purely thermal model and ignore the non-thermal electrons for the dynamics. Further justification of this assumption as well as implications of this constraint are discussed in §5.

We can obtain additional constraints on the parameters η and p in Sgr A* by studying the infrared data. Sgr A* is quiet at infrared wavelengths, with a current upper limit of 10^{35} erg s^{-1} on the luminosity at 2.2 μm (Eckart & Genzel 1997; Ghez et al. 1998). Since νL_ν decreases with increasing frequency for $p > 3$, we cannot use IR data to constrain η very strongly in these cases. On the other hand, if $p < 3$, electrons in an extended power-law distribution produce significant emission in the infrared. For example, if $p = 2.5$, we find that the maximum allowed fraction of energy in non-thermal electrons is $\eta = 0.05\%$. Tighter bounds on the infrared flux will constrain the parameters η and p even more strongly.

We note that imposing a maximum Lorentz factor $\gamma_{\rm max}$ on the power-law electron distribution also has the effect of suppressing the high-frequency emission. Therefore, for $p < 3$, we could alternatively use the IR data to constrain $\gamma_{\rm max}$ rather than η. The 2.2 μm emission is produced predominantly by electrons with $\log\gamma \gtrsim 3$ (see §4) placing a maximum Lorentz factor at $\gamma_{\rm max} \sim 10^3$, if $p < 3$ and $\eta > 0.05\%$.

Finally, we have considered ADAF models with strong outflows following the ideas described in Blandford & Begelman (1999), Di Matteo et al. (1999), and Quataert & Narayan (1999). We find that the constraints on η and $\gamma_{\rm max}$ obtained above do not depend strongly on the presence of winds.

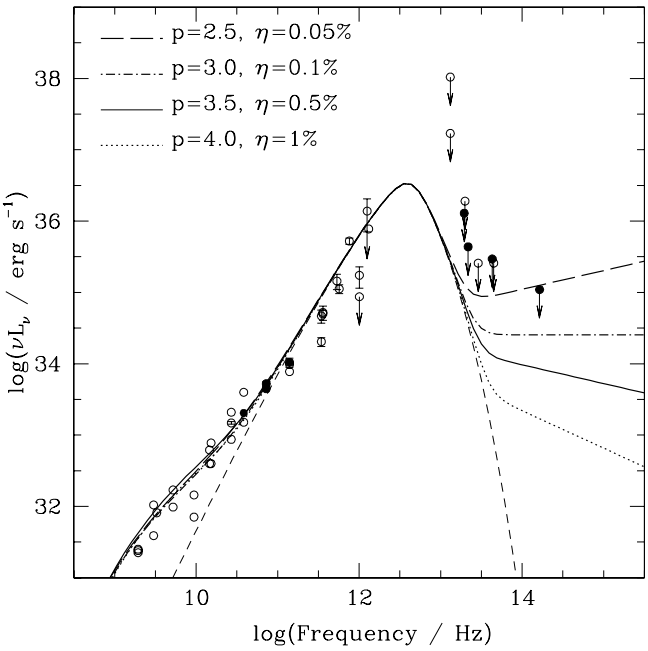

Fig. 4.— Comparison of spectral models for Sgr A* with radio and IR data. The dashed curve shows the spectrum when the electrons are purely thermal. The other four curves show spectra from hybrid populations with the following combinations of parameters: $p = 2.5$, $\eta = 0.05\%$; $p = 3.0$, $\eta = 0.2\%$; $p = 3.5$, $\eta = 0.5\%$, and $p = 4.0$, $\eta = 1\%$.

3.3. Image sizes and shapes

We now investigate the effect of a power-law electron population on the size and shape of the radio image of an ADAF. As a typical example, we consider an ADAF model of Sgr A* with $m_6 = 2.5$ and $\dot{m}_{-3} = 0.1$ and take a hybrid electron distribution with $p = 3.5$, $\eta = 0.5\%$ which agrees well with the observed spectrum as shown in Figure 4. Preliminary size measurements of Sgr A* are available at two frequencies (Lo et al. 1998, Krichbaum et al. 1998) and shape measurements may be possible in the near future. We note that although we use the parameters for a specific source, the qualitative results apply equally well to other massive black holes with different accretion rates.

We define the image size as twice the radial distance from the center of the image to the point at which the specific intensity falls to half the value of the central intensity, i.e., the FWHM of the radio map. Figure 5 shows the predicted FWHM of the image as a function of frequency. The dashed curve corresponds to the case when all the electrons are thermal and the solid line to the case of a hybrid energy distribution. The two data points for Sgr A* are from Lo et al. (1998) at 7 mm and Krichbaum et al. (1998) at 1.4 mm. Note that our radiative transfer code is one dimensional and can only handle spherical models, though ADAFs in general are oblate

and are likely to appear elliptical in projection (Narayan & Yi 1995a). In the comparison with observations, we use only the measured long axes of the images.

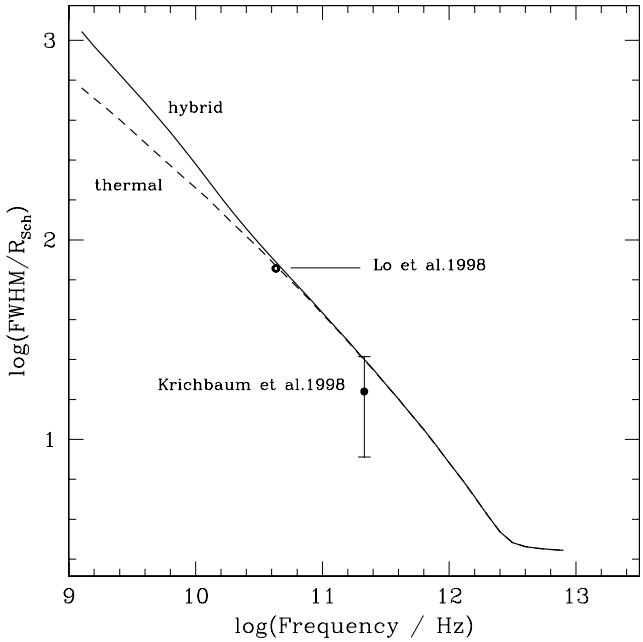

Fig. 5.— The solid line shows the FWHM image size corresponding to one of the models described in Figure 4, with $p = 3.5$ and $\eta = 0.5\%$. This is compared with two size measurements of the Galactic Center source Sgr A* at 1.4mm ($\nu = 214$ GHz) and 7mm ($\nu = 43$GHz). We do not show error bars of the 7mm measurement (Lo et al. 1998) because of the oblateness of the observed image which we have not included in our models. The dashed line corresponds to a pure thermal model.

The effect of power-law electrons is to enlarge the image size at long wavelengths ($\nu < 10^{11}$Hz), where the excess non-thermal emission, which extends outward of the surface of unit optical depth, is most prominent. This is a general result which holds true for all model parameters we have studied. The other related result is the steepening of the dependence of the image size on the frequency at long wavelengths. While for thermal electrons we find

$$\mathrm{FWHM/R_{Sch}} \sim \lambda^{0.7}, \tag{27}$$

when we include power law electrons, we find

$$\mathrm{FWHM/R_{Sch}} \sim \lambda^{0.9}. \tag{28}$$

This is in agreement with the preliminary result obtained by Lo et al. (1998) when they combined their measurement of the intrinsic size at 7 mm with the results of Krichbaum et al. (1998) at 1.4 mm, although the thermal and hybrid slopes are not distinguishable with the current data.

We also calculate the effective brightness temperature T_b at each frequency as $T_b = L_\nu c^2/(8\pi^2 k_B \nu^2 \mathrm{FWHM}^2)$. Figure 6 shows the result. For the thermal model, T_b

measures the electron temperature at the photosphere. Since the photosphere moves out with decreasing frequency, the brightness temperature falls. For the hybrid model, at lower frequencies, the contribution of the non-thermal electrons is large, the spectrum is non-thermal, and the resulting brightness temperature increases. This is another clear signature of a synchrotron-emitting hybrid electron population.

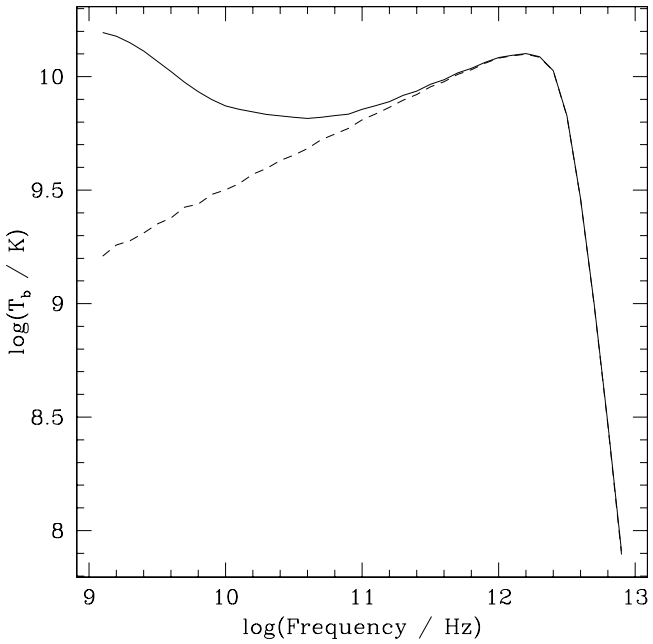

Fig. 6.— The predicted brightness temperature of Sgr A* as a function of frequency. The flux was taken from Figure 4 and the size estimate from Figure 5. The dashed line corresponds to the purely thermal model and the solid line to a hybrid model with $p = 3.5$ and $\eta = 0.5\%$.

We finally study the effect of the non-thermal electrons on the shape of the radio image. Figure 7 shows the variation of the brightness temperature T_b across the source, for the thermal and hybrid models of Sgr A* described above. We consider two wavelengths, 3.6 cm and 7 mm. The most striking feature of the hybrid case is the limb brightening seen at long wavelengths, a feature which is absent in the thermal models. Thus, if the accretion flow contains non-thermal electrons, its image would look like a shell rather than a disk. This is again due to the different radial dependences of absorption (which is predominantly thermal) and emission (which is mostly non-thermal) at the frequencies where the non-thermal shoulder appears in the energy spectrum. Because the total absorption falls off more steeply away from the center than the total emissivity, the image appears brighter for a range of impact parameters away from the center than at the center. In addition, due to the overall increase in the intensity of the emerging radiation in this same frequency range, the image looks brighter overall, with the brightness temperature T_b of the hybrid case increasing to twice the thermal value in the center of the image at 3.6 cm. The limb brightening, along with the enhanced overall brightness at long wavelengths are signatures of a

non-thermal population which may be accessible to observations. Unfortunately, in the case of Sgr A*, precisely at the wavelengths where the effects are strongest, interstellar scattering blurs the observed image (e.g., Lo et al. 1998). It may be worthwhile to look for these effects in other sources where the scattering is less severe.

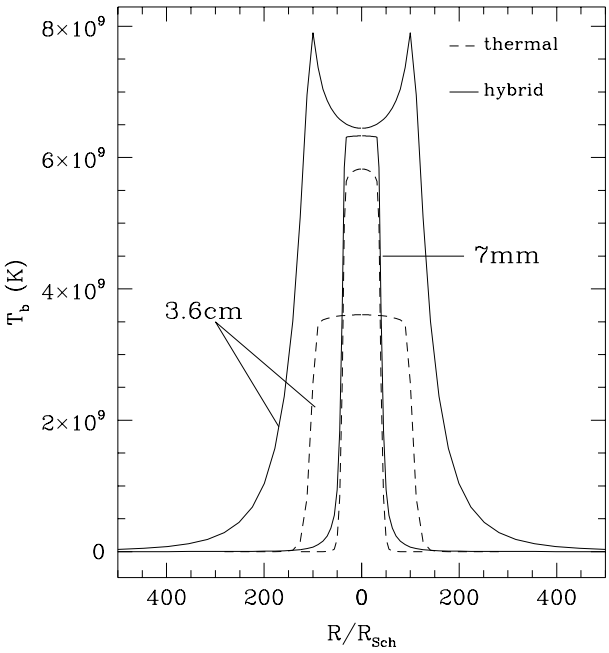

Fig. 7.— The predicted image shape of Sgr A* at 7mm and 3.6cm. The dashed line corresponds to the purely thermal model and the solid line to the hybrid model with $\eta = 0.5\%$ and p=3.5. Note that the hybrid model has a higher brightness temperature at both wavelengths, and is significantly limb-brightened at 3.6cm.

4. Electron Energy Distributions and the Shape of Synchrotron Spectra

The numerical studies presented in §3 show that the presence of a small population of power-law electrons causes universal modifications to the spectrum: it introduces a shoulder at low frequencies and a power-law tail at high frequencies. We now attempt to associate each of these features of the hybrid spectrum with a specific range of Lorentz factors of the non-thermal electrons. In doing so, we address three important issues.

The first is the question of degeneracy: why is the low frequency shoulder in the spectrum degenerate to a combination of the power-law index p and the energy content η of the non-thermal electrons? Understanding the source of non-uniqueness is especially important in trying to extract the underlying electron distributions from spectral data and determining what we can conclude *uniquely* about these distributions.

Second, since introducing even a very small fraction of power-law electrons results in significant enhancement of the luminosity at low frequencies, existing radio data can be used to constrain the non-thermal energy fraction in these accretion flows. If only a part of the electron energy distribution is responsible for the excess emission, data can further constrain these specific parts of the particle distribution.

The third question we address here is related to the absence of significant IR emission from the accretion flow around Sgr A* (Eckart & Genzel 1997), in the frequency range where the extended optically-thin non-thermal emission is expected. Absence of emission at these wavelengths provides information about the underlying electron distributions by constraining either the power-law index p or the maximum Lorentz factor γ_{max} electrons can attain in these accretion flows. Determining γ_{max} in a particle distribution may provide a better understanding of particle acceleration and cooling processes and timescales in hot accretion flows.

4.1. Correspondence between electron distributions and photon spectra

We first investigate the relationship between the Lorentz factor γ of an electron and the dominant frequency of the synchrotron emission it produces in the presence of a dominant thermal electron population. At very low frequencies, synchrotron emission comes from large radii in the flow where the temperatures are low, the non-thermal emission and absorption are efficient, and $\alpha_{\rm pl} \simeq \alpha_{\rm th}$. However, at higher frequencies near and above the low-frequency shoulder in the spectrum, $\alpha_{\rm th} \gg \alpha_{\rm pl}$, as discussed earlier. For these frequencies, we can thus neglect $\alpha_{\rm pl}$. We make this key simplification only in this section. It simplifies the radiative transfer equation and allows us to compute separately the contribution to the intensity from each value of γ in the non-thermal distribution.

We proceed by writing all quantities as integrals over the power-law electron distribution,

$$j_{\rm pl} = \int n_e^{\rm pl}(r,\gamma) j(\gamma) d\gamma, \tag{29}$$

$$I(\nu) \equiv \int n_e^{\rm pl}(\gamma) I_\gamma(\gamma) d\gamma, \tag{30}$$

and

$$j_{\rm th} = \frac{\int j_{\rm th} n_e^{\rm pl}(\gamma) d\gamma}{\int n_e^{\rm pl}(\gamma) d\gamma}, \tag{31}$$

where $n_e^{\rm pl}(r,\gamma)$ is assumed to be a separable function of r and γ given by

$$n_e^{\rm pl}(r,\gamma) = n_r^{\rm pl}(r) n_\gamma^{\rm pl}(\gamma) = N_{\rm pl}(r)(p-1)\gamma^{-p}. \tag{32}$$

(Note that, for this analysis, the non-thermal distribution does not have to be a power-law, though we have assumed this in order to compare this analysis directly to our numerical results).

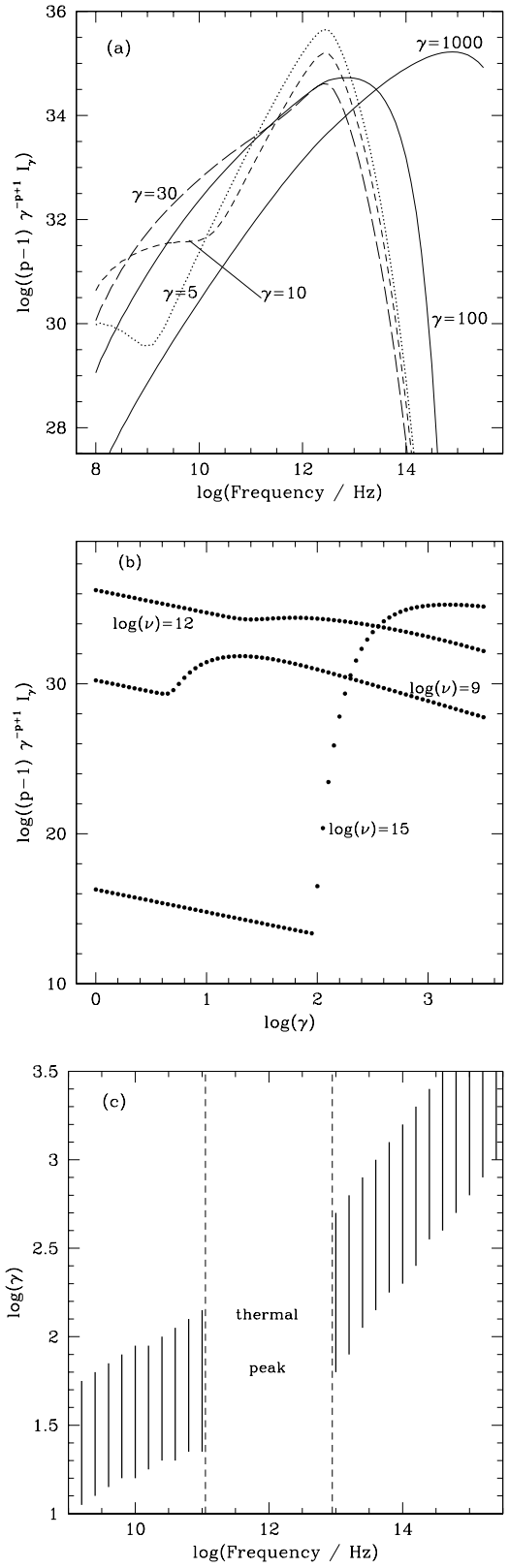

Fig. 8.— (a) The contributions to the hybrid spectrum of individual electron Lorentz factors: $\gamma = 5, 10, 30, 100,$ and 1000. (b) The range of Lorentz factors contributing to the emission at 10^9 Hz (low-frequency shoulder), 10^{12} Hz (thermal peak) and 10^{15} Hz (high-frequency tail). (c) A further quantification of (b) showing the minimum and maximum Lorentz factors at which the integrand falls to half its maximum value at each frequency.

Substituting equations (29)-(32) into the radiative transfer equation and rearranging terms, we obtain

$$\int [\mu \frac{\partial I_\gamma(\gamma)}{\partial x} + \alpha_{\rm th}(r) I_\gamma(\gamma) - n_r^{\rm pl}(r) j_\gamma(\gamma) - j_{\rm th}]\ n_\gamma^{\rm pl}(\gamma) d\gamma = 0. \quad (33)$$

For this integral to vanish for any non-thermal electron distribution, the integrand must be identically zero, thus giving

$$\mu \frac{\partial I_\gamma(\gamma)}{\partial x} = -\alpha_{\rm th}(r) I_\gamma(\gamma) + n_r^{\rm pl}(r) j_\gamma(\gamma) + j_{\rm th}. \quad (34)$$

We solve this equation for a wide range of Lorentz factors, $\log\gamma = 0.1 - 3.6$, by choosing a specific radial profile of the non-thermal electron density $N_{\rm pl}(r)$ corresponding to $p = 3.5, \eta = 0.5\%$. We study the contribution of each Lorentz factor to the different parts of the spectra. The total intensity for the power-law distribution takes the form

$$I(\nu) \equiv (p-1) \int \gamma^{-p+1} I_\gamma(\gamma) d(\log\gamma), \quad (35)$$

and therefore, in order to study the true contribution of each γ to the total spectrum, we plot the integrand $\gamma^{-p+1} I_\gamma(\gamma)$ as a function of frequency for each Lorentz factor. The result for $\gamma = 5, 10, 30, 100,$ and 1000 (for $p = 3.5$) are shown in Figure 8a. The curves give a good estimate of the individual contribution of each Lorentz factor to the total spectrum. Most of the contribution to the low-frequency shoulder comes from electrons with $\gamma \sim 30 - 50$. Emission from electrons with $\gamma \sim 100$ is already lower by an order of magnitude at those frequencies, and the emission completely dies off beyond $\gamma = 100$. Contribution to the high-frequency tail, on the other hand, starts around $\gamma \approx 100$ and increases with increasing electron energy.

To get a more quantitative idea of which range of Lorentz factors contributes to the three distinct regions of the spectrum, we show in Figure 8b the above integrand as a function of γ for 3 frequencies, namely 10^9 Hz (in the low-frequency shoulder), 10^{12} Hz (in the thermal peak), and 10^{15} Hz (in the high-frequency tail. We see that the emission at 10^9 Hz is primarily from electrons with $\gamma \sim 10^{1.5}$; the emission at 10^{12} Hz is mostly from $\gamma \sim 1$ (thermal electrons, while the emission at 10^{15} Hz comes mostly from $\gamma \gtrsim 10^2$.

To quantify this effect further, we plot in Figure 8c the minimum and maximum Lorentz factors for which the value of the integrand drops to half its maximum value for each frequency. This gives us exactly the contributing range of Lorentz factors to the emission at each frequency in the low-frequency shoulder and the high-frequency tail.

We may summarize the results as follows. The low-frequency shoulder is caused by a narrow range of electron Lorentz factors, $\log\gamma \sim 1 - 2$. The narrowness of the range explains why the spectra are degenerate to different combinations of p and η: a power-law distribution with small values of p and small η has nearly the same number of electrons in this narrow range of Lorentz factors as one with a larger p and a larger η, thus producing the same emission in the shoulder. The high-frequency tail, however, is produced by electrons with a wide range of Lorentz factors

($\log\gamma \gtrsim 2$) with higher frequencies coming from higher γ. Intermediate Lorentz factors $\log\gamma \sim 2$ emit predominantly at frequencies around the thermal peak and are overpowered by the thermal emission, and therefore do not have an observable feature in the hybrid spectrum.

5. Energetics of the thermal and non-thermal populations

In this section, we study the energy flow through the thermal and non-thermal electron populations as well as the energy exchange between these two populations through synchrotron self-absorption and Coulomb collisions. Starting with the energy equations for the two populations and a parametrization of the energy input into each, we calculate the steady-state energy content of both as a function of radius assuming that the shapes of the distributions are known a priori. Note that if the acceleration mechanism is known, the particle distributions can be calculated exactly (see, e.g., Nayakshin & Melia 1998). Here we simply assess the feasibility of a steady-state thermal/power-law hybrid distribution. We then extend our discussion of hybrid synchrotron spectra to cases where the parameter η is not constant but is allowed to vary with radius.

5.1. Energy Equations

We start by writing the energy equations for the two populations. Neglecting advection and diffusion which we estimate to be minor corrections, the energy balance for the power-law population reads

$$\frac{\partial E_{\rm nt}}{\partial t} = 0 = \delta_{\rm nt}\dot{E}_{\rm visc}(r) - \int j_{\rm nt}(\eta, p, r) d\nu d\Omega - \frac{E_{\rm nt}}{t_{ee}}, \tag{36}$$

while the thermal population obeys

$$\frac{\partial E_{\rm th}}{\partial t} = 0 = \delta\dot{E}_{\rm visc}(r) - \int \alpha_{\rm th}(B_\nu - I_\nu) d\nu d\Omega + \frac{E_{\rm nt}}{t_{ee}}, \tag{37}$$

where $E_{\rm th}$ and $E_{\rm nt}$ are the steady state energy contents of the thermal and power-law populations respectively, δ is the fraction of viscous energy that heats the thermal electrons, and $\delta_{\rm nt}$ is the corresponding fraction injected into the power-law population ($\delta_{\rm nt} = \eta_{\rm inj}\delta$, where $\eta_{\rm inj}$ is defined in §2.2); the time derivatives are set to zero in steady-state. The energy exchange (thermalization) timescale due to Coulomb collisions of high energy electrons with the thermal bath is denoted by t_{ee}. The radiation term in equation (36) corresponds to the energy loss by the non-thermal electrons via optically thin synchrotron emission; because the non-thermal absorption coefficient is negligible throughout the flow, the non-thermal electrons do not gain energy by absorption of synchrotron radiation. The corresponding term in equation (37), on the other hand, describes the heating of the thermal electrons by the local radiation field that is in excess of the blackbody limit. When the radiation energy density is a blackbody, there is locally no heating or cooling, but as the radiation energy density is above this limit due to emission by the non-thermal electrons, the

thermal electrons are heated by absorbing this total emission. Note that this is the same energy exchange mechanism invoked in the synchrotron boiler process (Ghisellini, Guilbert, & Svensson 1988; Ghisellini, Haardt, & Fabian 1993; Ghisellini, Haardt, & Svensson 1998). The transport of energy due to non-local synchrotron self-absorption is likely to be small and have little effect on the spectra as the photon mean free path becomes very short very rapidly along a radial path and thus the radiation emitted in the optically thick regions of the flow is reabsorbed locally. This is due to the very steep radial dependence of the synchrotron absorption coefficient.

There are several issues we would like to address regarding the relative importance of thermal and non-thermal electrons in the flow and the energy exchange between the two populations. First, the quantity $[\delta_{\rm nt}/\delta](r)$ determines as a function of radius the relative rate of heating of non-thermal electrons compared to thermal electrons. Second, the energy exchange between the populations (heating of the thermal electrons by non-thermal electrons) proceeds both via the Coulomb term and the absorption of the synchrotron photons emitted by the power-law populations (the second term of equation (37). Therefore the magnitude of these terms relative to the viscous heating of the thermal electrons needs to be assessed. Finally, the importance of the thermalization of the power-law distribution due to the Coulomb term also needs to be understood.

We first estimate the relative magnitude of the terms in equation (36). The ratio of the energy loss of the power-law electrons due to Coulomb collisions (the last term) to the energy emitted in synchrotron photons (the second to last term) determines whether Coulomb collisions or synchrotron self-absorption is the dominant mechanism by which the non-thermal electrons cool. The hybrid spectra presented in this paper have been computed under the assumption that the power-law electrons lose energy primarily through synchrotron emission, and this needs to be checked for consistency. For a given electron velocity β in the power-law distribution, the energy exchange rate with the thermal electrons is given by (Nayakshin & Melia 1998)

$$\left(\frac{dE}{dt}\right)_{ee} \simeq \frac{3}{2}\frac{\ln\Lambda}{t_T}\frac{1}{\beta\gamma_{\rm av}}, \tag{38}$$

where $\ln\Lambda \approx 20$ is the Coulomb logarithm, $\gamma_{\rm av}$ is the average thermal Lorentz factor, $t_T \equiv (n_e c\sigma_T)^{-1}$ is the Thomson mean-free time and n_e the electron density. The rate of energy loss of an electron of Lorentz factor γ emitting synchrotron radiation in a region of magnetic field B is (Rybicki & Lightman 1979)

$$\left(\frac{E}{t_{1/2}}\right)_{\rm syn} \simeq \frac{2e^4B^2\gamma^2}{3m^2c^3}, \tag{39}$$

where $t_{1/2}$ is the time for the electron to lose half its energy. Using the analytic expressions for the electron density and magnetic field strength given in §2.1 and substituting values for the coefficients and parameters appropriate for Sgr A*, we find for an electron of a given γ:

$$\frac{(dE/dt)_{ee}}{(E/t_{1/2})_{\rm syn}} \approx 0.1r\gamma^{-2}, \tag{40}$$

where r is the radius in Scwarzschild units as usual. Most of the emission in the low-frequency shoulder in the spectrum originates from around $r \simeq 100$ and the radiation is produced by

electrons with $\gamma \simeq 50$ (cf. Fig. 8c and the Appendix). We thus see that the ratio in equation (40) is at most a few percent. This shows that Coulomb collisions play a negligible role in the cooling of non-thermal electrons. It also shows that that the heating of thermal electrons by Coulomb collisions is unimportant compared to energy exchange via synchrotron emission and absorption. We therefore neglect the Coulomb term in the following calculations.

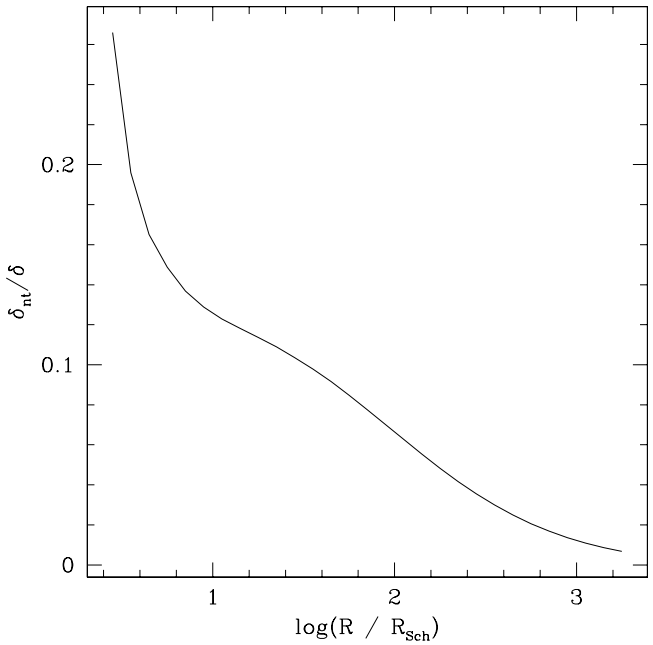

Fig. 9.— The ratio of the non-thermal electron heating parameter $\delta_{\rm nt}$ to the thermal electron heating parameter δ as a function of radius for a model of Sgr A* with $p = 3.5$, $\eta = 0.5\%$.

The power-law electrons then obey a simple energy balance between the injected energy through viscous dissipation and the energy loss through synchrotron emission. The latter simply is the total frequency- and angle-integrated synchrotron emissivity of the non-thermal electrons because this population is optically thin to synchrotron emission. Therefore, once $\delta_{\rm nt}(r)$ is specified, it is possible to calculate the parameter η, which describes the steady-state energy content of the power-law electrons, as a function of radius. Conversely, if we specify $\eta(r)$ as we did in the previous sections, it is possible to compute the energy $\delta_{\rm nt}$ that would need to be injected into the non-thermal electrons as a function of radius. We first study the latter case for $\eta =$ constant, as this is the assumption we have made in most of this paper. Figure 9 shows $\delta_{\rm nt}/\delta$ as a function of radius for one of the hybrid models of Sgr A* with $\eta = 0.5\%$, and $p = 3.5$. The figure demonstrates that the energy input into the non-thermal electrons never exceeds 20% of the heating of the thermal electrons and in fact does not exceed 10% at those radii that contribute to the low-frequency shoulder in the spectrum ($10R_s < R < 1000R_s$). Thus, at no radius in the flow do the power-law electrons become energetically more important than, or even comparable

to, the thermal electrons. This may seem like a surprising result considering that the non-thermal radiation clearly dominates over the thermal emission in the low-frequency shoulder of the spectrum and in the high-frequency tail. However, the synchrotron emissivities of the thermal and power-law populations are different by many orders of magnitude at these frequencies. (Optically thin synchrotron emission from a power-law population peaks at a much higher intensity and at a lower frequency than the thermal emission for the same energy density and magnetic field strength.) Therefore, even when the non-thermal population has less energy content than the thermal population, and even when a fraction of the non-thermal radiation is absorbed by the thermal electrons at frequencies where the flow is optically thick, the escaping radiation can still be dominated by the non-thermal emission and the intensity can be much above the blackbody limit. This is the situation in the low-frequency shoulder of the spectrum. In the high-frequency tail, the only particles that are energetic enough to produce the radiation are the non-thermal electrons, and since the flow is optically thin all the radiation escapes freely. Incidentally, the fact that the energy input into the non-thermal electrons does not exceed 20% of the heating of the thermal electrons (and even this level is reached only over a small range of radius close to the black hole) shows that the dynamics of the flow is not affected by the presence of non-thermal electrons.

We also consider the other mechanism of energy exchange between the two populations, namely synchrotron self-absorption by thermal electrons. The second term in equation (36) measures the maximum energy that can be radiated by the non-thermal electrons as a function of radius. This term also represents an upper limit on the energy that can be transferred to the thermal population via self-absorption. This term is bounded from above by $\delta_{\rm nt}\dot{E}_{\rm visc}$ according to equation (36). Since $\delta_{\rm nt}/\delta$ never exceeds 20% as shown in figure 9, heating of the thermal electrons by absorbing synchrotron emission from non-thermal electrons can *at most* introduce a 20% correction to the thermal energy equation; the correction is only a few percent at large radius. This again justifies neglecting the contribution of the non-thermal electrons to the thermodynamic properties of the flow.

Finally we note that the calculations in the previous sections considered a simple parametrization of the non-thermal population via the quantity η, which measures the fraction of the electron energy in steady state that is present in non-thermal electrons. Now, η is a secondary quantity whose value depends on the balance between non-thermal heating and cooling. It would perhaps be more useful to parametrize the model by specifying the non-thermal heating parameter $\delta_{\rm nt}$. To this end, we consider models in which the energy injection rate varies as a power-law in radius, $\delta_{\rm nt} \propto r^{-q}$, and show results for q between 0 and 1. We pick the normalization of $\delta_{\rm nt}$ at the inner edge of the flow such that the resulting $\eta(r)$ is comparable to the values used in §3 and is in accord with the results of Figure 9. In Figure 10a, we show $\eta(r)$ for $p = 3.5$ and three different choices of q: 0, 1/2, and 3/4. For none of the three cases do we see very large variations in the resulting $\eta(r)$ versus radius; we find that $\eta(r)$ rises with radius for $q \lesssim 1/2$ and falls for larger values of q. Figure 10b shows the spectra corresponding to the three models of $\delta_{\rm nt}$. We see that the two universal features of a hybrid spectrum, the low-frequency shoulder and the

high-energy tail, are present for all values of q. Thus, super-thermal emission is not an artifact of specific assumptions or parameter values of our models but is indeed a robust signature of a hybrid population. The slope of the low-frequency shoulder depends very mildly on the particular model of $\delta(r)$.

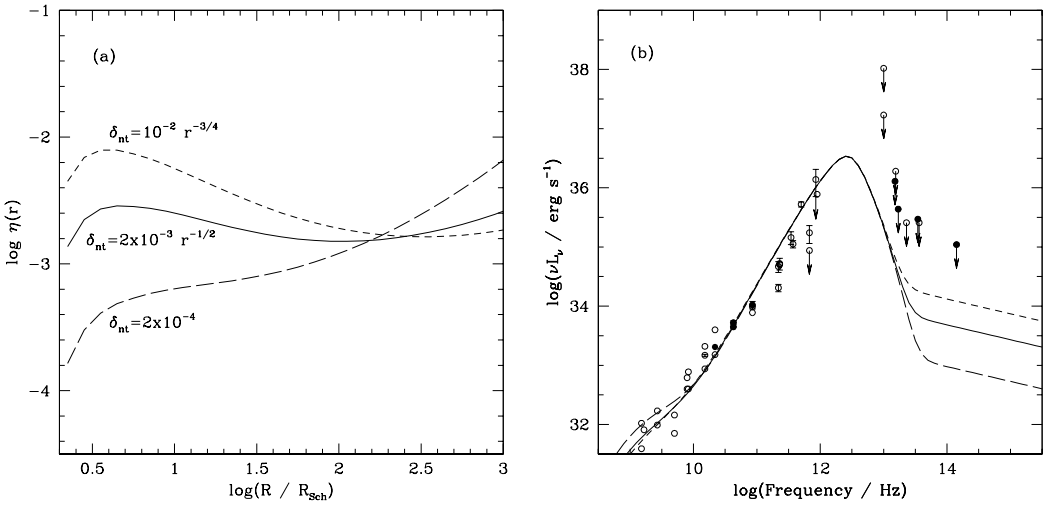

Fig. 10.— (a) The steady-state non-thermal energy content $\eta(r)$ corresponding to three models of the non-thermal energy injection rate, $\delta_{\rm nt} \propto r^{-q}$, with $q = 0$, 1/2, and 1. All the models have $p = 3.5$. (b) Spectra corresponding to the same three models, compared with data on Sgr A*.

6. Discussion

In this paper we considered hot accretion flows around supermassive black holes, using the ADAF model as a typical example. Such hot flows are expected to occur at low mass-accretion rates. We assume that a fraction of the viscous dissipation energy in the accretion flow goes into accelerating electrons to a non-thermal power-law distribution. We find that a power-law tail of high energy electrons can be sustained in such flows; neither Coulomb collisions nor synchrotron self-absorption is able to thermalize the power-law electrons. Assuming that there are no other thermalizing mechanisms (e.g., collective plasma modes), we calculate the resulting hybrid thermal/non-thermal spectrum from such a plasma.

The presence of even a population of non-thermal electrons gives rise to two universal and prominent features in the synchrotron spectrum: a low-frequency shoulder and a high-frequency tail (Fig. 2). These features were identified by Mahadevan (1998) who considered a specific mechanism (via pion decay) for the production of power-law electrons. Even if only a small fraction of the total steady-state electron energy is in the non-thermal power-law component, we find that there is significant super-thermal emission in the low-frequency shoulder and the high

frequency tail of the spectrum. Furthermore, each of these universal features can be associated with a specific range of Lorentz factors of the emitting electrons. The low-frequency shoulder is emitted by electrons with Lorentz factors $\log \gamma = 1 - 2$, while the high-energy tail is emitted by electrons with $\log \gamma \gtrsim 2$ (Fig.8).

Since the power-law electrons cause significant emission at low frequencies, comparing this low-frequency shoulder to data can provide stringent constraints on the fraction of the electron energy that is present in a non-thermal population. In the case of Sgr A* (Fig. 4), we conclude that, in steady-state, electrons even with intermediate Lorentz factors (γ as low as 10) make up only a very small fraction of the electron population. Since Coulomb collisions and synchrotron self-absorption are ineffective in thermalizing these flows, this means that either the energy injected into a non-thermal population, $\delta_{\rm nt}\dot{E}_{\rm visc}$, is small as in the calculations described in §5 or there is some other efficient thermalization mechanism which plays a role in these flows. The study on Sgr A* needs to be extended to other sources before we can judge how universal the result is.

Here it is important to emphasize two points regarding the constraints on non-thermal electrons obtained from the spectrum.

First, for the part of the spectrum below the thermal peak, there is a mapping between each frequency in the spectrum and the thin shell of radii which predominantly emits at that frequency. This is due to the steep radial dependence of the synchrotron absorption that causes a sharp transition between optically thick and optically thin regions in the flow. Therefore, emission at each frequency comes primarily from a specific radius in the flow and can be used to probe the non-thermal content in a shell that extends from that radius out to a somewhat larger radius. (Mathematically, radiation emerging at each frequency comes from the entire range from the radius where the optical depth is unity out to infinity, but because the total emissivity also drops rapidly with radius, the biggest contribution to the intensity integral comes from a relatively narrow shell). As a result, the constraints on the non-thermal distribution obtained from each frequency of the low-frequency shoulder apply only to electrons within this shell. Inside the radius corresponding to optical depth unity, the emission is heavily self-absorbed and the electron distribution there is inaccessible to observations.

Second, the constraints on the non-thermal energy content which we have obtained for Sgr A* would not be invalidated if the observed low-frequency shoulder originated in a separate, extended region such as a jet or an outflow exterior to the accretion flow. In that case, the observed fluxes may be treated as upper limits to the emission from the inner accretion flow. This would imply that the non-thermal emission from the accretion flow is even smaller than in our models and the resulting constraints on the fraction of non-thermal electrons would become only tighter.

When the non-thermal electron distribution is a power law, three parameters of the model and three corresponding pieces of physics can be extracted by comparing hybrid emission models to spectral data. The first parameter is η, or equivalently $\delta_{\rm nt}$ (cf.§5), which measures the fraction of the dissipated energy that goes into the non-thermal electrons. The second parameter is p, the

slope of the power-law energy distribution (eq. 4). This can be uniquely determined by measuring the spectral slope of the high-frequency tail in the spectrum (provided there is no competing emission via Compton scattering at these wavelengths, cf. Fig. 1). The value of p may provide an indication of the mechanism by which the electrons in a hot accretion flow are accelerated into a power-law tail. The third parameter, which is more significant for distributions with $p < 3$, is $\gamma_{\rm max}$, the maximum Lorentz factor to which electrons are accelerated. If this parameter can be determined by an IR cutoff in the spectrum, it would provide information on the ratio of the acceleration timescale to the synchrotron cooling timescale.

Due to the degeneracy of the low-frequency shoulder to the parameters η and p (Fig. 4), this segment of the spectrum by itself is not sufficient to constrain the two parameters. However, η and p may be determined uniquely if we have information on both the low-frequency shoulder and the high-frequency tail. For this to work, there should be no contamination from a jet or outflow to the observed radiation in the low-frequency shoulder or from Compton scattering in the high frequency tail.

We showed in this paper that the presence of a non-thermal population of electrons also has measurable effects on the shape of the image of the source, and the size of the accretion flow, as a function of frequency (Figs. 5-7). Because the frequency dependence of the image size is strongly affected by the fraction of non-thermal electrons in the flow, measuring the size of accretion flows at multiple wavelengths can provide a quantitative constraint on the non-thermal electron energy content. Moreover, the brightness temperature of the source as a whole, as well as the variation of the brightness temperature across the source, at long wavelengths behave differently for a hybrid plasma compared to a purely thermal population of electrons. Finally, at the frequencies corresponding to the low-frequency shoulder, we show that there would be limb brightening of the image. All these image-related signatures may help to identify the presence of a non-thermal population of electrons, and the parameters of the corresponding energy distribution.

We thank Eliot Quataert, Anthony Aguirre, Tiziana Di Matteo, and James Cho for many useful discussions and comments on the manuscript. We also thank S. Nayakshin, the referee, for many useful comments and suggestions that improved the presentation of the paper. D. P. was supported by a post-doctoral fellowship of the Smithsonian Institution. This work was supported in part by NSF Grant AST 9820686.

A. Analytic Approximations

In this appendix, we provide analytic formulae for the slope of the spectrum below and above the thermal peak and the relative importance of non-thermal electrons as a function of mass, accretion rate, power law index p, and non-thermal energy content η. For convenience, we use the self-similar solution of ADAFs to obtain these analytic estimates.

A.1. Self-Similar Advection-Dominated Flows

We begin by presenting the self-similar ADAF solution developed by Narayan & Yi (1994, 1995b). The self-similar solution describes the local properties of the accretion flow as a function of the black hole mass M, the mass accretion rate $\dot{M}$, the radius R, the viscosity parameter α, the ratio of gas pressure to the total pressure β, and the fraction of viscously dissipated energy that is advected inwards f.

In terms of the scalings introduced in §2.1, the height-averaged electron number density n_e, the magnetic field strength B, and the dimensionless proton temperature $\theta_p \equiv kT_p/m_pc^2$ of the accretion flow are:

$$n_e = n_1 m_6^{-1} \dot{m}_{-3} r^{-3/2} \text{ g cm}^{-3}, \tag{A1}$$

$$B = b_1 m_6^{-1/2} \dot{m}_{-3}^{1/2} r^{-5/4} \text{ G}, \tag{A2}$$

and

$$\theta_p = 0.18 \beta r^{-1}, \tag{A3}$$

where

$$n_1 = 2.0 \times 10^{10} \alpha^{-1} c_1^{-1} c_3^{-1/2}, \tag{A4}$$

and

$$b_1 = 2.07 \times 10^4 \alpha^{-1/2} (1-\beta)^{1/2} c_1^{-1/2} c_3^{1/4}. \tag{A5}$$

The coefficients c_1 and c_3 are defined in Narayan & Yi (1995b) and are related to the adiabatic index of the gas and the fraction of advected energy f. For the cases of interest here, $c_1 \simeq 0.5$ and $c_3 \simeq 0.3$. The remaining parameters were specified in §2.1.

A.2. Fundamental synchrotron quantities in self-similar ADAFs

We now use the self-similar solution to obtain expressions for the cyclotron frequency and the harmonic number for synchrotron emission. Since we focus our applications to galactic nuclei and very large mass black holes where the synchrotron frequencies of interest are in the radio regime, we scale the frequency as $\nu_{10} = \nu/10^{10}$. The magnetic field strength is then

$$B = 4.85 \times 10^4 m_6^{-1/2} \dot{m}_{-3}^{1/2} r^{-5/4} \tag{A6}$$

and thus fundamental cyclotron frequency defined in §2.3 becomes:

$$\nu_b = 1.4 \times 10^{11} m_6^{-1/2} \dot{m}_{-3}^{1/2} r^{-5/4} \tag{A7}$$

The ion temperature retains its virial value throughout the flow and is given, in dimensionless units $\theta_i = \frac{kT_i}{m_u c^2}$, by:

$$\theta_i = 0.61 \beta c_3 r^{-1} = 0.2 r^{-1} \tag{A8}$$

when we set the parameter values to those used in the simulations. The behaviour of the electron temperature on the other hand is more complicated and depends on the detailed balance of heating and cooling at each radius. Qualitatively, electron temperature starts out virial and equal to the ion temperature at large radii ($r = 10^5$), but increases less steeply than the ion temperature at smaller radii due to cooling by mainly synchrotron emission. Because it is not possible to derive the exact electron temperature as a function of radius analytically, we provide instead numerical fits to the average radial dependence of electron temperature

$$\theta_e = 1.65 \times r^{-0.6}. \tag{A9}$$

Since synchrotron absorption coefficient is a steep function of radius, we can assume that most of the optically thick emission comes from a narrow range of radii around the radius with optical depth equal to unity. Due to the complicated nature of the expression for the thermal synchrotron absorption which does not allow analytic integration, we numerically determine the dependence of this $\tau = 1$ radius, r_{t1} on mass, mass accretion rate and frequency. The best fit gives

$$r_{t1} = 2.5 \times 10^2 m_6^{-1/4} \dot{m}_{-3}^{1/3} \nu_{10}^{-0.6} \tag{A10}$$

Substituting r_{t1} into ν_b and θ_e we get

$$\nu_b = 1.4 \times 10^8 m_6^{-3/16} \dot{m}_{-3}^{1/12} \nu_{10}^{3/4} \tag{A11}$$

and

$$\theta_e = 0.06 \times m_6^{0.15} \dot{m}_{-3}^{-0.2} \nu_{10}^{0.36} \tag{A12}$$

Finally, we compute the harmonic number defined in §2.3:

$$x_M = \frac{2\nu}{3\nu_b \theta_e^2} \tag{A13}$$

$$x_M = 1.32 \times 10^4 m_6^{-0.1} \dot{m}_{-3}^{0.3} \nu_{10}^{-0.47} \tag{A14}$$

which provides all the necessary synchrotron expressions as a function of black hole mass, mass accretion rate and frequency.

A.3. Where does the non-thermal emission dominate: Normalization

We can now derive analytic estimates for the contribution of the non-thermal emission to the low-frequency shoulder and the high-frequency tail. In the optically thick shoulder, self-absorption of the synchrotron emission is done predominantly by the thermal electrons, and we find that absorption due to non-thermal electrons are negligible down to a frequency of $\nu \simeq 10^9$ as discussed above. Thus the source function will take the form

$$S_{\rm tot} = \frac{j_{\rm th}}{\alpha_{\rm th}} + \frac{j_{\rm pl}}{\alpha_{\rm th}} \tag{A15}$$

where $j_{\rm th}$ is synchrotron emissivity per unit volume given in §2.3.

For the analytic approximations, we will use a simplified form of the thermal emissivity. We first take the fully relativistic limit derived first by Pacholczyk, which is equivalent to setting a, b and c equal to 1 in $M(x_M)$. We further neglect the second and third terms of the sum altogether by setting b and c equal to zero as these terms provide only a very small correction unimportant for the present purposes. Thus, in simplified form, the ratio of the two emissivities is given by

$$\frac{j_{\rm pl}}{j_{\rm th}} = \eta C'_{\rm pl} a(\theta) K_2(1/\theta)\theta(\frac{\nu}{\nu_b})^{-(p+1)/2} x_M^{1/6} \exp(1.9 x_M^{1/3}) \tag{A16}$$

where

$$C'_{\rm pl} = \frac{\sqrt{3} C_{\rm pl}}{4} \tag{A17}$$

and all other quantities are as defined as before.

The non-thermal emission dominates over the thermal emission in the spectrum when $j_{\rm pl}/j_{\rm th} > 1$. This ratio can be easily computed using the expressions for x_M, θ_e, and ν_b evaluated at the $\tau = 1$ radius given above.

The power law emission beyond the thermal peak is optically thin and hence the excess in this region depends sensitively on the power-law index as expected and is simply given by the optically thin synchrotron emission from the power-law electrons. The amount of emission is determined simply by $j_{\rm pl}$.

We finally note that, for the small values of η considered here, thermal emission dominates at the thermal peak. The strong dependence of the position and the normalization of the thermal peak on m and $\dot{m}$ is discussed by Mahadevan (1997).

A.4. Spectral Slope

The shape of the low-frequency shoulder is dominated by the emission of the power-law population and absorption by the thermal electrons. In order to determine the spectral slope of this segment, we therefore first calculate the hybrid source function

$$S_\nu = j_{\rm pl}/\alpha_{\rm th} \tag{A18}$$

at the surface of unit optical depth. To convert this into a luminosity, we multiply the source function by the area of the $\tau = 1$ surface. If we write the shoulder of the spectrum as $\nu L_\nu \propto \nu^s$, the spectral slope s is then given by

$$s = 2.5 - p/8 - 7.2\dot{m}_{-3}^{0.1}\nu_{10}^{-0.16} + 6m_6^{-0.15}\dot{m}_{-3}^{0.2}\nu_{10}^{-0.36} \tag{A19}$$

which gives the canonical value of $\sim 4/3$ for the mass and mass-accretion rate of Sgr A* and scales (weakly) according to the expression above for other masses and accretion rates. One can

immediately see that the spectral slope depends very weakly on p, only as $p/8$, thus demonstrating again the independence of the spectral slope of the low-frequency shoulder on the shape of the electron energy distribution.

The slope of the optically thin power law emission is a well-known result,

$$s = -(p-3)/2 \tag{A20}$$

which in νL_ν for $p < 3$, flat for p=3 and falls off for $p > 3$. It is independent of the black hole mass and the accretion rate.

REFERENCES

Abramowicz, M. A., Chen, X. , Kato, S. , Lasota, J. -P. & Regev, O. 1995, ApJ, 438, L37

Beckert, T. & Duschl, W. J. 1997, A&A, 328, 95

Begelman, M. C. & Chiueh, T. 1988, ApJ, 332, 872

Bisnovatyi-Kogan, G. S. & Lovelace, R. V. E. 1997, ApJ, 486, L43

Blandford, R. D. & Begelman, M. C. 1999, MNRAS, 303, L1

Chandrasekhar, S. 1939, Introduction to the Study of Stellar Structure (Chicago: The University of Chicago Press)

Chen, X. , Abramowicz, M. A. & Lasota, J. -P. 1997, ApJ, 476, 61

Coppi, P. S. 1999, in High Energy Processes in Accreting Black Holes, ASP Conference Series 161, Eds. Juri Poutanen & Roland Svensson.

Di Matteo, T., Fabian, A. C., Rees, M. J., Carilli, C. L. & Ivison, R. J. 1999, MNRAS, 305, 492

Eckart, A. & Genzel, R. 1997, MNRAS, 284, 576

Falcke, H. & Biermann, P. L. 1999, A&A, 342, 49

Gammie, C. F. & Popham, R. 1998, ApJ, 498, 313

Ghez, A. M., Klein, B. L., Morris, M. & Becklin, E. E. 1998, ApJ, 509, 678

Ghisellini, G. , Guilbert, P. W. & Svensson, R. 1988, ApJ, 334, L5

Ghisellini, G., Haardt, F. & Fabian, A. C. 1993, MNRAS, 263, L9

Ghisellini, G., Haardt, F. & Svensson, R. 1998, MNRAS, 297, 348

Gruzinov, A. & Quataert, E. 1999, ApJ, 520, 849

Ichimaru, S. 1977, ApJ, 214, 840

Kato, S., Fukue, J. & Mineshige, S. 1998, Black-hole Accretion Disks (Kyoto: Kyoto University Press)

Krichbaum, T. P., et al. 1998, A&A, 335, L106

Lo, K. Y., Shen, Z. -Q. , Zhao, J. -H. & Ho, P. T. P. 1998, ApJ, 508, L61

Lovelace, R. V. E., Romanova, M. M. & Bisnovatyi-Kogan, G. S. 1999, ApJ, 514, 368

Mahadevan, R. 1997, ApJ, 477, 585

———. 1998, Nature, 394, 651

———. 1999, MNRAS, 304, 501

Mahadevan, R. , Narayan, R. & Yi, I. 1996, ApJ, 465, 327

Mahadevan, R. & Quataert, E. 1997, ApJ, 490, 605

Melia, F. 1992, ApJ, 387, L25

Mihalas, D. 1978, Stellar Atmospheres (San Francisco: Freeman)

Narayan, R. , Barret, D. & MCClintock, J. E. 1997a, ApJ, 482, 448

Narayan, R. , Kato, S. & Honma, F. 1997b, ApJ, 476, 49

Narayan, R., Mahadevan, R., Grindlay, J. E., Popham, R. G. & Gammie, C. 1998a, ApJ, 492, 554

Narayan, R., Mahadevan, R. & Quataert, E. 1998b, in Theory of Black Hole Accretion Disks, Eds. M. Abramowicz, G. Bjornsson, and J. Pringle (Cambridge: Cambridge University Press)

Narayan, R. & Yi, I. 1994, ApJ, 428, L13

———. 1995a, ApJ, 444, 231

———. 1995b, ApJ, 452, 710

Narayan, R., Yi, I. & Mahadevan, R. 1995, Nature, 374, 623

Nayakshin, S. & Melia, F. 1998, ApJS, 114, 269

Pacholczyk, A. G. 1970, Radio Astrophysics, (San Francisco: Freeman)

Petrosian, V. 1981, ApJ, 251, 727

Popham, R. & Gammie, C. F. 1998, ApJ, 504, 419

Quataert, E. & Gruzinov, A. 1999, ApJ, 520, 248

Quataert, E. & Narayan, R. 1999, ApJ, 520, 298

Rybicki, G. B. & Lightman, A. P. 1979, Radiative Processes in Astrophysics (New York: Wiley-Interscience)